Imaging beyond the Born approximation: An experimental investigation with an ultrasonic ring array

F. Simonetti*
Department of Mechanical Engineering, Imperial College, London SW7 2AZ, United Kingdom and MS D443, Los Alamos National Laboratory, Los Alamos, New Mexico 87545, USA

L. Huang
MS D443, Los Alamos National Laboratory, Los Alamos, New Mexico 87545, USA

N. Duric and O. Rama
Karmanos Cancer Institute, Wayne State University, 4100 John R, Detroit, Michigan 48201, USA
(Received 31 October 2006; revised manuscript received 27 April 2007; published 4 September 2007)

The classical diffraction limit excludes the possibility of resolving features of an object which are spaced less than half a wavelength apart when scattering experiments are performed from the far field. However, recently it has been shown that this limit could be a consequence of the Born approximation that neglects the distortion of the probing wave as it travels through the object to be imaged. Such a distortion, which is due to the multiple scattering phenomenon, can encode unlimited resolution in the radiating component of the scattered field thus leading to super resolution. In this context, a resolution better than $\lambda/3$ has been reported in the case of elastic wave probing [F. Simonetti, Phys. Rev. E **73**, 036619 (2006)], λ being the wavelength of the wave illuminating the object. This paper demonstrates a resolution better than $\lambda/4$ and approaching $\lambda/6$ for objects immersed in a water bath probed by means of a ring transducer array that excites and detects ultrasonic pressure waves in a full view configuration. This is achieved despite the presence of a high level of noise in the measurements (the signal to noise ratio was below 0 dB). Moreover, while previous papers have provided experimental evidence of super resolution for objects small compared to the wavelength, here the case of extended objects is also investigated.

DOI: 10.1103/PhysRevE.76.036601 PACS number(s): 42.30.−d, 43.60.+d, 95.75.Mn

I. INTRODUCTION

Physical models that govern the interaction between waves, either mechanical or electromagnetic, and matter provide a formidable tool to infer the properties of an object. In this context and for a long time, the Born approximation has represented the fundamental building block for a number of imaging techniques employed in medical diagnostics, radar surveillance, geophysical exploration, and nondestructive testing.

The Born approximation leads to a simplified scattering model that neglects the distortion of the probing wave induced by the structure of the object as the wave travels through it. As a result, the scattered field can be thought of as a superposition of a continuous distribution of elementary scattering events that take place at different points within the object and are independent of each other, implying that multiple scattering, which would interlink different events, is neglected. From a mathematical standpoint, this leads to a linear integral mapping which links the object structure to the scattered field and vice versa. Although the Born approximation provides a simple and direct method to reconstruct the structure of an object from the measurement of the scattered field, features of the object which are spaced less than $\lambda/2$ apart, where λ is wavelength of the probing wave, cannot be resolved [1]. This is ultimately due to the presence of noise in the actual measurements as explained in Ref. [2] and references therein.

The major implication of the $\lambda/2$ resolution limit is that short wavelengths need to be propagated in order to achieve high resolution; however, short wavelengths are usually characterized by a large attenuation with propagation distance due to material absorption and scattering. Therefore, in general resolution has to be traded against penetration depth.

In a recent paper under the general framework of the *T*-matrix formalism [3], it has been shown that thanks to the presence of multiple scattering, the radiating component of the scattered field does indeed contain unlimited resolution information about the structure of the scattering object. However, while the link between the measurements and object structure is linear under the Born approximation, the mapping becomes nonlinear in the case of multiple scattering. This nonlinearity represents the major challenge in subwavelength imaging from far field measurements since in order to reconstruct the object a nonlinear inverse problem has to be solved. This is known as the inverse scattering problem and although the solution exists and is unique (at least when the object can be illuminated from all the directions contained in the solid angle 4π), the problem is ill-posed in the sense of Hadamard [4] due to the instability of the solution which does not vary continuously with the input (measurements).

Understanding and controlling the ill-posedness of the inverse scattering problem is a fundamental step towards the development of a robust imaging technology. In this context, regularization techniques and a careful design of the archi-

*f.simonetti@imperial.ac.uk

tecture of the hardware used to collect the measurements play a crucial role. For instance, sensor array systems, which have undergone a tremendous development over the past years thanks to progress in solid state physics and telecommunications, can limit the ill-posedness by increasing the number of independent measurements and by reducing the noise characteristics of individual sensors which ultimately trigger the instability. Clearly, the validity of these arguments has to be supported by experimental evidence to test the stability of the inversion against realistic measurement errors. The experimental work on subwavelength imaging by Chen and Chew [5] using electromagnetic waves in the microwave regime and that by Simonetti using elastic waves in plates [3] and three dimensional solids [6] provide strong evidence about the feasibility of such an approach.

The aim of this paper is to show that by taking into account multiple scattering a stable inversion of the scattering problem can be achieved in the presence of large experimental errors or noise and that subwavelength resolution is possible in practice. Based on the ideas introduced in Ref. [3], experimental evidence is provided by means of a prototype ring array consisting of 256 sensors which excite and detect pressure waves in a water bath. The system provides a full view configuration enabling insonification of an object from regular angular intervals around it. An imaging algorithm based on the eigenfunction analysis of the far-field operator, which can directly be measured by means of the array, is investigated. This type of approach was first pursued by Lin *et al.* [7] in the framework of the Born approximation. In contrast, the study presented in this paper addresses the factorization method (FM), which belongs to the class of the so-called linear sampling methods developed over the past two decades by Colton, Kirsch, and several other authors (for a recent review, see Ref. [8]). These methods are very attractive because they provide a direct solution to the nonlinear inverse scattering problem, in contrast with iterative methods of gradient or Newton type which are computationally expensive and often require an initial guess about the scatterer structure. Although there exists a vast literature on the theoretical aspects of these methods, little experimental work has been done. Results for extended objects (characteristic size larger than λ) have only been reported by Kirsch [9] who applied the FM to the microwave measurements part of the Ipswich dataset [10]. Images of subwavelength objects obtained by using flexural waves in plates and bulk waves in a steel block have been reported by Simonetti [3,6]. In this paper, an unprecedented resolution of $\lambda/4$ and approaching $\lambda/6$ for an object located at approximately 70λ distance from the sensors is demonstrated. This is a remarkable result considered the high level of noise present in the measurements (the signal-to-noise ratio was below 0 dB). Moreover, it is shown experimentally that the FM can be applied to the shape reconstruction of extended scatterers probed with pressure waves.

The scattering model is described in Sec. II which introduces the principal properties of the far-field operator that is central to the FM as discussed in Sec. III. Section IV describes the experimental setup and the procedure to extract the far-field operator from the measurements. The results for three different sets of experiments are reported in Sec. V.

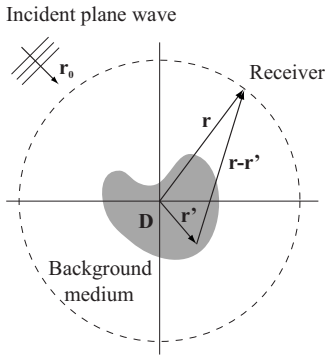

FIG. 1. A plane wave is incident on an object immersed in a homogeneous background medium. The field scattered by the object is measured with sensors placed in the far field.

II. THEORETICAL BACKGROUND

Let us consider the scattering problem depicted in Fig. 1 in which a plane wave is incident on an object and the scattered field is measured by means of sensors deployed around it. The object is immersed in a homogeneous background medium through which the incident and scattered waves propagate. In this paper it is assumed that the scattering problem is described by a monochromatic scalar wave field, $\psi(\mathbf{r},k\hat{\mathbf{r}}_0)$ which has the asymptotic form

$$\lim_{r\to\infty}\psi(\mathbf{r},k\hat{\mathbf{r}}_0)=e^{ik\hat{\mathbf{r}}_0\cdot\mathbf{r}}+f(k\hat{\mathbf{r}},k\hat{\mathbf{r}}_0)\frac{e^{ikr}}{r}, \tag{1}$$

where the first term of the right-hand side is the incident plane wave of wave number $k=2\pi/\lambda$ that illuminates the object and $f(k\hat{\mathbf{r}},k\hat{\mathbf{r}}_0)$ is the scattering amplitude defined as

$$f(k\hat{\mathbf{r}},k\hat{\mathbf{r}}_0)=\frac{k^2}{4\pi}\int_D d^3r' e^{-ik\hat{\mathbf{r}}\cdot\mathbf{r}'}O(\mathbf{r}')\psi(\mathbf{r}',k\hat{\mathbf{r}}_0). \tag{2}$$

$O(\mathbf{r})$ is a function of support D corresponding to the volume occupied by the object and is known as the "*object function*." $O(\mathbf{r})$ is related to the index of refraction, $n(\mathbf{r})$, through the relationship $O(\mathbf{r})=n^2(\mathbf{r})-1$ [11].

The scattering amplitude can be measured experimentally, by illuminating the object from all possible directions $\hat{\mathbf{r}}_0$ and for each of them detecting the scattered field in all directions $\hat{\mathbf{r}}$, both illumination and detection being performed in the far field. Under the Born approximation, it is assumed that the total field, $\psi(\mathbf{r}',k\hat{\mathbf{r}}_0)$ in Eq. (2), can be approximated by the incident field leading to

$$f_{\mathrm{BA}}(k\hat{\mathbf{r}},k\hat{\mathbf{r}}_0)=\frac{k^2}{4\pi}\int_D d^3r' e^{-ik(\hat{\mathbf{r}}-\hat{\mathbf{r}}_0)\cdot\mathbf{r}'}O(\mathbf{r}'), \tag{3}$$

which is proportional to the spatial Fourier transform of the object function calculated at the point $k(\hat{\mathbf{r}}-\hat{\mathbf{r}}_0)$ of the K-space [12]. Therefore, Eq. (3) provides a linear mapping between $O(\mathbf{r})$ and the far-field measurements. Moreover, the inverse scattering problem can easily be solved by applying the inverse Fourier transform to the scattering amplitude. On the other hand, in the general case of multiple scattering, Eq. (2)

is no longer a linear mapping and a different inversion strategy needs to be used.

In this paper, a nonlinear inverse methods which can reconstruct the support of $O(\mathbf{r})$, i.e., the external shape of the scatterer, is considered. The method is based on the far-field operator, $T_\infty: L^2(\mathbb{S}) \to L^2(\mathbb{S})$

$$T_\infty|y\rangle = \int_{\mathbb{S}} ds(\hat{\mathbf{r}}_0) f(k\hat{\mathbf{r}}, k\hat{\mathbf{r}}_0) y(k\hat{\mathbf{r}}_0), \tag{4}$$

where $\mathbb{S}$ is the unit shell in $\mathbb{R}^3$ and the Ket symbol is used according to the Dirac bra-ket notation [13]. The physical interpretation of T_∞ is that $T_\infty|y\rangle$ is the far-field pattern of the scattered field due to a linear combination of incident plane waves, $\exp(ik\hat{\mathbf{r}}_0 \cdot \mathbf{z})$, with relative amplitude $y(k\hat{\mathbf{r}}_0)$, $\mathbf{z}$ being a point in space illuminated by the incident wave. As shown by Gerjuoy and Saxon [14], T_∞ can be related to the scattering matrix, S, which links the incoming component of the total field to the outgoing one, according to the relationship

$$S = I + \frac{ik}{2\pi} T_\infty, \tag{5}$$

where I is the identity operator. The properties of the scattering matrix have long been studied in quantum mechanics and a number of textbooks cover the subject (see, for instance, Ref. [15]). In particular, in nonabsorbing media, S is normal, $SS^\dagger = S^\dagger S$ ($S^\dagger$ is the adjoint operator of S), by energy conservation, and Eq. (5) implies that also T_∞ is normal. Moreover, it can be shown that T_∞ is compact [16] and therefore has a countable number of discrete eigenvalues accumulating only at zero. As a result, there exists an orthonormal basis $\{v^n\}$ for $L^2(\mathbb{S})$ consisting of eigenfunctions of T_∞

$$T_\infty|v^n\rangle = \mu_n|v^n\rangle, \tag{6}$$

or equivalently

$$T_\infty^\dagger T_\infty|v^n\rangle = |\mu_n|^2|v^n\rangle, \tag{7}$$

which means that $\{|\mu_n|, |v^n\rangle, \mathrm{sgn}(\mu_n)|v^n\rangle\}$ is a singular system for T_∞. As an example, for two-dimensional problems and radially symmetric objects, the scattering amplitude only depends on the angle θ formed between the illumination and detection directions, therefore as observed by Lin *et al.* [7] the eigenfunctions have the form

$$|v^n\rangle = \frac{1}{\sqrt{2\pi}} e^{in\theta}, \quad \forall\, n \in \mathbb{Z} \tag{8}$$

and the eigenvalues are given by

$$\mu_n = \int_0^{2\pi} d\theta\, f(\theta) e^{in\theta}, \tag{9}$$

which implies that the eigenvalues are the coefficients of the cylindrical wave expansion of the scattering amplitude $f(\theta)$ (note that the scattering amplitude no longer depends on the individual values of $k\hat{\mathbf{r}}$ and $k\hat{\mathbf{r}}_0$, but on θ only).

Equation (9) leads to an important observation when the object is a pointlike scatterer. In this case, the scattered field is an outgoing cylindrical wave and all the coefficients of the cylindrical wave expansion vanish except the coefficient corresponding to the zero order; as a result, only one nonzero eigenvalue exists. More generally, for a finite number of pointlike scatterers, M, the number of nonzero eigenvalues is M [17]. On the other hand, if the size of the scatterer is not negligible compared to the wavelength (extended scatterers), none of the eigenvalues vanish. As an example, let us consider the case of an impenetrable circular cylinder, it can be shown that the scattered field is given by

$$\psi^s(\theta, r) = \sum_{n=-\infty}^{+\infty} i^n a_n H_n^{(1)}(kr) e^{in\theta}, \tag{10}$$

where $H_n^{(1)}$ are the nth order Hankel functions of the first kind which describe outward propagating waves. Alternatively, Eq. (10) can be expanded in the sum of an optical reflection and infinite fluid-borne surface waves known as creeping waves or Franz waves, which circumnavigate the cylinder and interfere with the optical reflection causing resonances [18]. The coefficients a_n in Eq. (10) depend on the boundary condition at the interface between the cylinder and the surrounding medium. For a sound-soft object which corresponds to a void in the medium the Dirichlet conditions holds whereas, if the cylinder is rigid (sound hard) the Neumann condition is required. The coefficients have the form

$$a_n = \begin{cases} -J_n(ka)/H_n^{(1)}(ka) & \text{Dirichlet}, \\ -J_n'(ka)/H_n'^{(1)}(ka) & \text{Neumann}, \end{cases} \tag{11}$$

where J_n is the nth order Bessel function of the first kind and a is the cylinder radius. For a two-dimensional problem the scattering amplitude is defined as

$$f(\theta) = \lim_{r \to \infty} \psi^s(\theta, r) \sqrt{r} e^{-ikr}, \tag{12}$$

hence from Eq. (10) using the asymptotic form of the Hankel functions the scattering amplitude for a circular cylinder is

$$f(\theta) = \sqrt{\frac{2}{i\pi k}} \sum_{n=-\infty}^{+\infty} a_n e^{in\theta}. \tag{13}$$

As a result, by substituting Eq. (13) into Eq. (9) the eigenvalues are

$$\mu_n = \sqrt{\frac{8\pi}{ki}} a_n, \tag{14}$$

which due to the normality of T_∞ lie on a circle of the complex plane passing through the origin with radius $\sqrt{2\pi/k}$ and centered along the line $\mathrm{Im}\{\mu\} = -\mathrm{Re}\{\mu\}$, with $\mathrm{Im}\{\mu\} > 0$. This is a general property and applies to any two-dimensional nonabsorbing object; see, for instance, Ref. [19].

The expression of the coefficients a_n in Eq. (11) along with the structure of the Hankel and Bessel functions implies that the eigenvalues μ_n corresponding to $|n| < ka$ have dominant magnitude compared to the others. This can be deduced from Fig. 2 which provides the coefficient a_{60} for a sound-hard cylinder as a function of the product ka. The physical explanation for this upper bound lies in the fact that ka corresponds to the number of wavelengths contained in the circumference of the cylinder. Any field with a larger number of

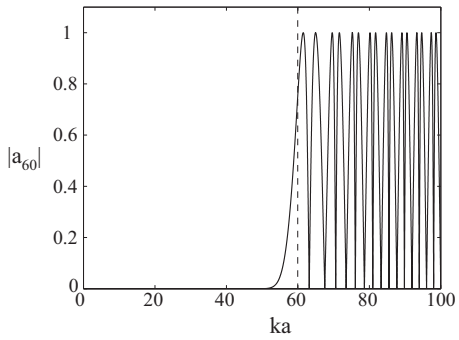

FIG. 2. Coefficient a_{60} for a sound-hard cylinder as a function of ka. The coefficient is small when $ka<60$ whereas it assumes any value in [0 1] for $ka>60$.

oscillations ($|n|>ka$) cannot reach the far-field since the background medium cannot support the propagation of a field whose spatial fluctuations occur over a scale shorter than λ. This applies to objects of any shape, where now a is the radius of the circle which circumscribes the object; for a more detailed discussion see Ref. [20]. As a result, for a given radius and wavelength the maximum number of dominant eigenvalues is $\approx 2ka+1$. Figure 3(a) shows the eigenvalues of a sound-hard cylinder ($a/\lambda=5$) normalized with respect to the largest eigenvalue for $-128<n<128$, among these≈60 eigenvalues have dominant amplitude, as clearly seen in Fig. 3(b) which shows the same eigenvalues ordered from the largest to the lowest. Note that the scale is now semilogarithmic and only the eigenvalues larger than 10^{-20} are shown. The same graph also shows the eigenstructures for a small cylinder ($a/\lambda=0.5$) and a large one ($a/\lambda=10$).

III. FACTORIZATION METHOD

The FM is one of the linear sampling methods used for shape reconstruction and was proposed by Kirsch in 1998 [21] who considered the equation

$$(T_\infty^\dagger T_\infty)^{1/4}|y_{\mathbf{z}}\rangle = |g_{\mathbf{z}}\rangle, \tag{15}$$

where $T_\infty^\dagger$ is the adjoint of T_∞ in $L^2(\mathbb{S})$ and where the function $g_{\mathbf{z}} \in L^2(\mathbb{S})$ is the steering function defined as

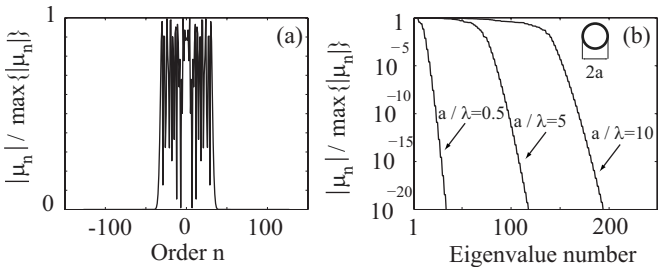

FIG. 3. Eigenvalue structure of the far-field operator calculated for a sound-hard circular cylinder: (a) Normalized eigenvalues corresponding to $-128<n<128$ for $a/\lambda=5$; (b) eigenvalues reordered from the largest to the lowest for three different radius to wavelength ratios.

$$g_{\mathbf{z}}(k\hat{\mathbf{r}}) = e^{-ik\hat{\mathbf{r}}\cdot\mathbf{z}}. \tag{16}$$

Kirsch showed that for lossless media, a point $\mathbf{z}$ belongs to D if and only if Eq. (15) is solvable. By means of Picard's theorem, this implies that the support of the object function, D, is the locus of points $\mathbf{z}$ for which

$$\mathbf{z} \in D \Leftrightarrow P(\mathbf{z}) = \left(\sum_{n=1}^{\infty} \frac{1}{|\mu_n|} |\langle g_{\mathbf{z}} | v^n \rangle|^2 \right)^{-1} > 0, \tag{17}$$

where $P(\mathbf{z})$ is referred to as a pseudospectrum. The shape of the object can then be reconstructed by evaluating the functional $P(\mathbf{z})$ over a grid of $\mathbb{R}^3$ or $\mathbb{R}^2$ depending on whether a three- or two-dimensional problem is considered. Note that neither the Born approximation nor particular boundary conditions on ∂D are assumed.

IV. EXPERIMENTS

The experiments were performed with an ultrasonic ring array developed at the Karmanos Cancer Institute, Wayne State University, for breast imaging. The array consists of 256 transducer elements mounted on a circular ring with an internal diameter of 200 mm. The ring is immersed in water which provides the background medium. The center frequency of the elements is 1.3 MHz with ~100% bandwidth. The interelement spacing is 2.5 mm and the active area of each element is 0.5×12 mm^2, with the long side of the element being perpendicular to the ring plane. The system excites all 256 channels sequentially and for each transmission all the transducers record the total pressure field. Therefore, all the possible transmit and receive combinations that can be acquired with different transducer pairs of the array are measured. This leads to 65 536 time traces for a total of around 100 MBytes of integer data depending on the duration of each recoding. The total acquisition time required to collect the 65 536 time traces is in the order of 0.3 s.

Measurement of T_∞

Due to the finite size and number of sensors only a discretized version of the far-field operator can be measured. This leads to what is known as the multistatic matrix, K, whose i-j entry is the scattered field recorded by the element i when element j transmits. Since the signal recorded by each transducer is proportional to the total field, i.e., incident plus scattered fields, the scattering amplitude is obtained by subtracting the incident field from the total field, the incident field being measured before immersing the object in the water bath. As pointed out by Lin *et al.* [7] the subtraction approach relies on the temperature of water being constant during the two sets of measurements, temperature variations as little as 1 K can lead to large phase shifts which cause large errors when the incident field is subtracted from the total field. Although it is possible to compensate for these variations by monitoring the temperature, the very short acquisition time allows the two sets of measurements to be performed in a rapid succession to exclude the possibility of temperature changes.

The measurement of the incident field is also used to calibrate the array elements. Due to different electromechanical and geometrical properties of each element, the element response is not uniform across the array; the standard deviation of the element amplitude response was found to be ~30% of the average amplitude response.

After measuring the scattered field, the *i-j* entry of the multitsatic matrix at a prescribed frequency, ω, was obtained by performing the Fourier transform of the *i-j* time trace and selecting the complex value of the spectrum at the frequency ω.

It has to be mentioned that the scattering amplitude, hence the far-field operator, is defined for incident plane waves. However, the field excited by each array element is much more complicated than a plane wave due to the size of the element and the presence of neighboring transducers. To some extent the element could be considered as a line source which excites an omnidirectional cylindrical wave propagating in the plane of the array. This is justified by the large height of each element compared to the wavelength which limits the elevation angle of the ultrasound beam to less than 10° so confining the beam within the array plane. However, in the array plane, the beam is far from being omnidirectional because of the finite width of the elements ($\sim\lambda/2$) and the presence of neighboring transducers which make the beam strongly directional with an in-plane beam divergence of approximately 30°. However, for objects whose characteristic size is much smaller than the ring diameter and are placed in the vicinity of the array center, the incoming wave can be considered to be a plane wave.

Finally the interelement pitch, which is much larger than λ, causes circular grating lobes centered in the middle of the array. The first grating lobe has a maximum amplitude along a circle of radius $R_{\max}$ [20]

$$R_{\max} \simeq \frac{\lambda}{4\pi} N, \tag{18}$$

where N is the number of elements. For a 256 element array and $\lambda = 1$ mm, this leads to $R_{\max} \sim 20$ mm. In order to avoid artifacts, the imaging plane has to be limited to a disk of radius smaller than $R_{\max}$ concentric with the array.

V. RESULTS

Three different sets of two-dimensional experiments were performed to assess the capabilities of the FM under realistic noise. First, a circular rod of 30λ diameter was tested to demonstrate that the sampling methods can actually be used to image extended targets with pressure waves. Subsequently, a second set of experiments was performed with two nylon wires to further investigate the super resolving capabilities of the FM. Finally, by means of a two cylinder experiment it was shown that while reconstruction methods based on the Born approximation suffer from artifacts due to multiple scattering, the FM leads to images with much fewer artifacts.

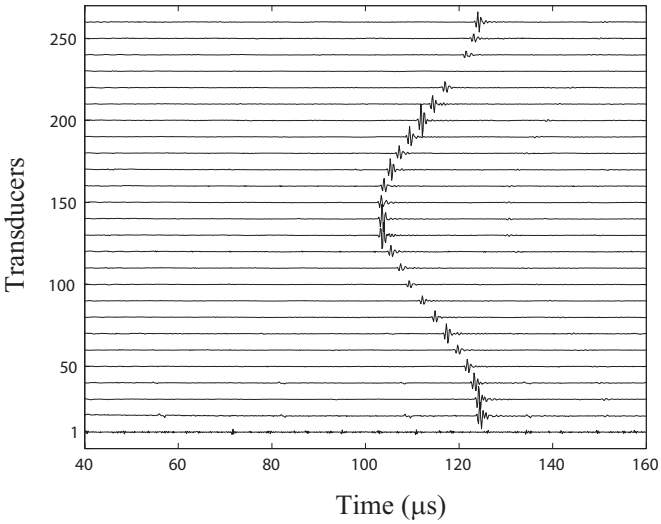

FIG. 4. Pulse-echo signals showing the reflection from a 34 mm diameter rod immersed in water.

A. Single rod experiment

A 34 mm diameter solid plastic rod was positioned in the proximity of the array center with its axis perpendicular to the array plane so as to simulate a two-dimensional problem.

Figure 4 shows some of the pulse-echo signals (transmit and receive with the same element) recoded by the array and used to build the T_∞ operator. Different arrival times are due to the eccentricity of the rod with respect to center of the ring. Nevertheless, the amplitude of the reflections should be the same for all the sensors. The variations are due to the different responses of the elements, which in some extreme cases are not functioning (see, for instance, element number one). It is not possible to provide a single figure to estimate the signal-to-noise ratio (SNR) because the signals vary with transmit-receive pairs. However, one possibility is to define an upper bound by considering the pulse echo signals, which for a circular scatterer correspond to the strongest signals. The SNR can then be defined as the ratio of the average amplitude of the reflection divided by the rms of the random noise, which for the case considered in Fig. 4 leads to an upper bound of 20 dB.

Figure 5 provides the eigenvalues of the measured T_∞ at 1.3 MHz, the plot being normalized with respect to the largest eigenvalue. The amplitude of the eigenvalues exhibits a sharp drop around the 180th eigenvalue which marks the transition from dominant to non-dominant eigenvalues. It should be emphasized that throughout this paper it is assumed that the wave field is described by a scalar potential. However, the objects considered in the experiments are solids and the actual wave field within the object is given by the superposition of a scalar and a vector potentials according to the standard Helmholtz decomposition [22]. The large impedance contrast between the rod and water ensures that little energy is transmitted through the rod. However, some of the energy travels in the form of surface waves which circumnavigate the cylinder and have energy both in the rod and in water. These waves are associated with the normal modes of

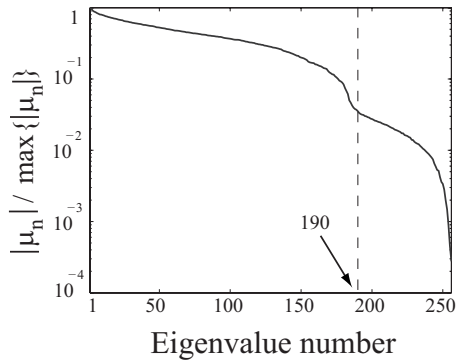

FIG. 5. Eigenvalue structure of the far-field operator for the 34 mm diameter rod at 1.3 MHz.

the immersed rod and are known as whispering gallery waves. Flax and Dragonette [23] have shown that in the case of an aluminium cylinder immersed in water, the coefficients of the partial wave expansion (10), hence the eigenvalues of the T_∞ operator, are the same as those of a sound-hard cylinder (see Fig. 2) with the exception of a finite number of frequencies ka where resonances occur. These are caused by the whispering gallery waves and occur when the cylinder circumference is an integer multiple of their wavelengths (for a comprehensive review of this topic, see Ref. [24]). However, for the cases considered in this paper these resonances can be neglected for two reasons. First, here only monochromatic reconstructions are considered; therefore, only the frequencies where resonances occur would be affected. Moreover, the resonances are weak as it can be deduced from the pulse-echo measurements shown in Fig. 4. Each time trace reveals the presence of a weak whispering gallery wave following the main specular reflection after 27 μs, this being the time required by the surface wave to go around the cylinder once. The low amplitude of the surface wave implies that the resonance is heavily damped, hence the object can effectively be treated as sound-hard. As a result, the number of dominant eigenvalues should be $\approx 2ka+1 \approx 185$ which matches well the experimental results shown in Fig. 5.

Figure 6(a) is a monochromatic image of the shape of the cylinder obtained with the FM by plotting the spectrum (17) at 1.3 MHz. The black dots represent the actual position of the array elements. The spectrum was calculated by truncating the series in Eq. (17) at $n=250$. The truncation provides a simple means to regularize the inverse problem. In particular, it can be observed that the eigenvalues, μ_n, appear at the denominator of the series; as a result, the smaller the eigenvalue the larger the amplification of errors contained in $|\langle g_{\mathbf{z}}|v^n\rangle|^2$. In other words, the truncation removes the contribution from the lowest eigenvalues and stabilizes the series.

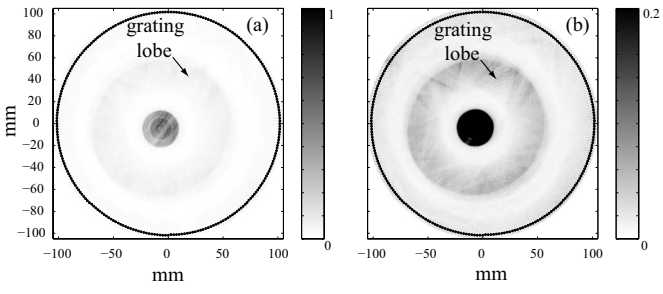

FIG. 6. Monochromatic images of a 34 mm diameter rod obtained with the factorization method at 1.3 MHz ($\lambda=1.16$ mm): (a) Before threshold; (b) after applying threshold. The dots along the circle represent the actual positions of the array elements.

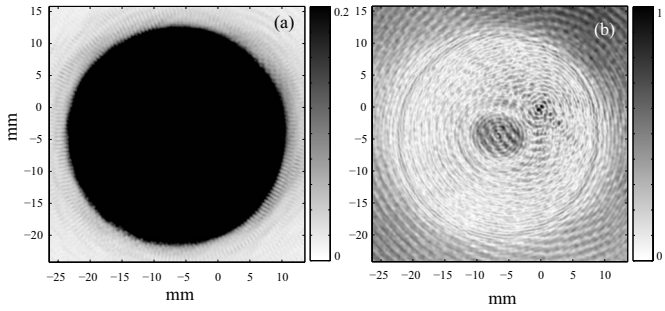

FIG. 7. Monochromatic images of a 34 mm diameter rod at 1.3 MHz ($\lambda=1.16$ mm) obtained with (a) factorization method; (b) Kirchhoff migration. Note that the color scales are different.

It can be noticed that, although the contour of the rod is very well defined, the image is not uniform along the rod cross section (the image is normalized with respect to the largest value of the spectrum) which exhibits concentric circles. This is due to the structure of the spectrum (17) and the discrete nature of the measurements as explained in the Appendix. However, this is of no concern because the image becomes homogenized by choosing a threshold level above which the color associated to the functional is the same regardless of its actual value, as long as the functional is above the threshold. This is shown in Fig. 6(b) where the threshold is set to be 20% of the maximum value. Note that the halo in the two images is a grating lobe due to the large interelement spacing. The halo occurs at a radius which is twice that provided by Eq. (18) because it corresponds to the zero order circumferential component of the scattered field, which in this case is dominant due to the strong symmetry of the problem. For a detailed discussion about the grating lobe structure, see Ref. [20].

Next, Fig. 7(a) provides a more detailed image of the contour of the rod previously shown in Fig. 6. Due to the presence of noise, some subwavelength ripples with a peak-to-peak amplitude of $\lambda/3$ can be observed along the bottom right side of the cylinder. The ripples cause an uncertainty in the radius estimate of around $\lambda/6$.

Figure 7(b) shows a reconstruction of the rod obtained with the Kirchhoff migration (KM) also known as summation migration [25] which here is defined according to

$$I(\mathbf{z}) = \langle g_{\mathbf{z}}|T_\infty|g_{\mathbf{z}}\rangle. \tag{19}$$

Equation (19) is usually integrated over the frequency bandwidth of the signal. While for limited view experiments (i.e., when the sensors do not surround the object) frequency diversity improves the range resolution [26], in the full view scenario considered in this paper, it does not enhance the resolution which is determined by the highest harmonic only

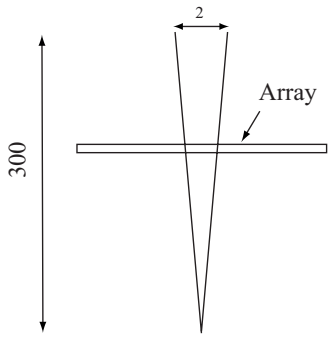

FIG. 8. Diagram of the setup used to control the spacing between the two nylon wires. The array is scanned vertically so as to illuminate the region with the desired spacing (dimensions are in mm).

[1]. KM is equivalent to synthetic phased arrays (also known as sum-and-delay beamforming) whereby an acoustic beam is focused and steered over the imaging plane [27]. The method is based on the Born approximation and does not take into account the distortion of the probing wave as it travels through the medium to be imaged. Clearly, the FM outperform the monochromatic KM method and provides much higher resolution and lower side lobes.

B. Two wire experiment

In order to assess the super resolving capabilities of the FM, an experiment employing two 0.25 mm diameter nylon wires was performed. The separation distance between the wires was controlled by spacing them 2 mm apart at one end and joining together the other end to form a very narrow V as shown in Fig. 8. The distance between the free ends of the wires and the junction point was 300 mm. By scanning the array vertically it was possible to illuminate different sections of the wires to achieve the desired spacing. Thanks to the relatively small angle between the wires ($\sim 0.4°$), they can be considered parallel within the slice illuminated by the array. However, care must be taken in orienting the plane containing the two wires perpendicularly to the array plane. Failure to do so would result in the obliquity of the wires with respect to the array and the problem can no longer be considered two-dimensional.

Due to the small diameter of the wires the reflected signal was very weak as it can be observed in Fig. 9 which shows some of the measured pulse-echo time traces. The arrival times of the reflections fall in the range of 120–140 μs. The reflections are buried in the background noise and the SNR is lower than 0 dB.

Figure 10 shows the eigenvalues of the measured far-field operator at 1 MHz. This frequency was selected because it provides a large wavelength, 1.5 mm, while maintaining a relatively high signal to noise ratio. In the present example, it was estimated that 15 eigenvalues were dominant using the empirical approach based on the slope of the eigenvalues described in Ref. [3]. Since the wires are small compared to λ (the diameter is $\lambda/6$), the number of dominant eigenvalues is expected to be small. In the limit for pointlike scatterers,

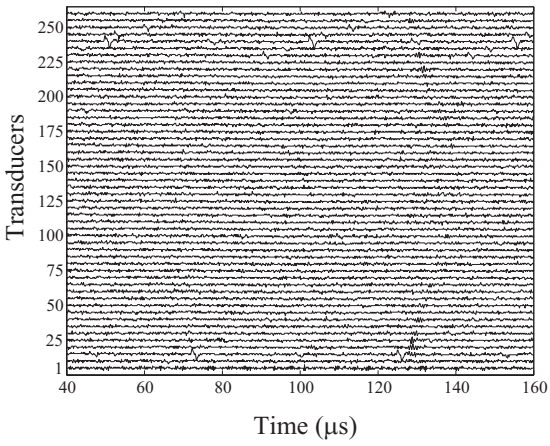

FIG. 9. Pulse-echo time traces measured for the two-nylon-wire experiment. Due to the small size of the wires, the reflected signals which occur between 120–140 μs are weak and buried in the background noise.

only two nonzero eigenvalues would exist. However, due to the $\lambda/6$ diameter of the wires the theory would predict three dominant eigenvalues associated with each wire $(2ka+1)$ thus resulting in a total of six dominant eigenvalues. The discrepancy between experimental and theoretical values is due to the presence of noise which increases the magnitude of the nondominant eigenvalues.

The position of the wires relative to the array is shown in Fig. 11 which was obtained with the FM. Figure 12(a) is an enlarged view of Fig. 11 over an area $\lambda \times \lambda$ around the wires. Due to large noise level, the Tikhonov regularization, based on the Morozov discrepancy principle [28], was used instead of the series truncation. The FM was able to resolve the two wires despite of their $\lambda/4$ spacing. Moreover, the FM leads to a well defined shape of the scatterers revealing features which are even smaller than $\lambda/4$. Note that the diameter of the wires is $\lambda/6$. This is a remarkable result given the low SNR of the measurements (see Fig. 9) and the large distance between the wires and the sensors $\sim 70\lambda$. On the other hand, the KM is not able to resolve the two wires as shown in Fig.

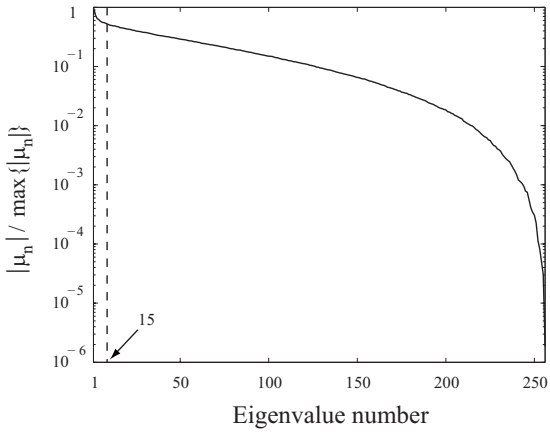

FIG. 10. Eigenvalues of the measured far-field operator at 1 MHz for the two-wire experiment.

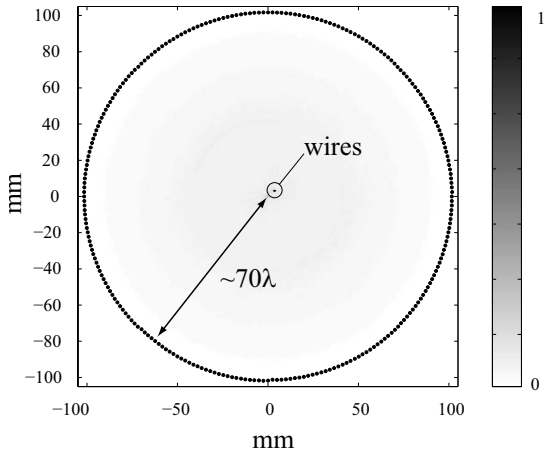

FIG. 11. Image of the two wires obtained with the FM showing their position relative to the array. The size of the pixels is $\lambda \times \lambda$.

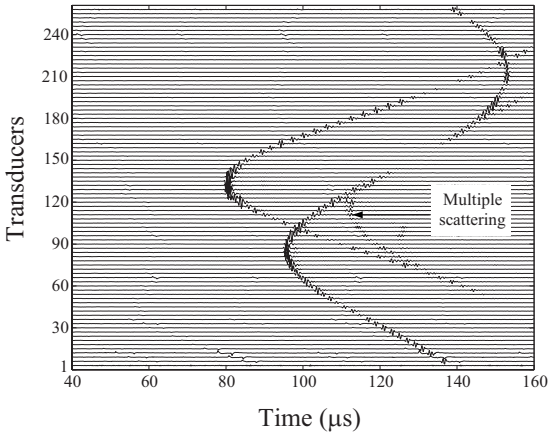

FIG. 13. Pulse-echo time traces measured for the two rod experiment. The presence of multiple scattering is revealed by the wave packet arriving after the two direct reflections.

12(b). The lack of resolution is not due to noise but to the intrinsic limitations of the Born approximation which leads to the $\lambda/2$ resolution limit.

C. Two rod experiment

The purpose of this experiment was to show that reconstruction algorithms based on the Born approximation suffer from severe artifact caused by multiple scattering. For this purpose two hollow glass rods, 17 mm in diameter with an interaxial separation of 34 mm were used. The rods were circumscribed by a circle of 40 mm radius concentric with the array. Therefore, in order to avoid the presence of grating lobes [Eq. (18)] the reconstruction used the T_∞ operator at 850 kHz. The presence of strong multiple scattering between the cylinders can be deduced from Fig. 13 which shows some of the pulse-echo time traces. In general, each trace contains three or more wave packets, the first two correspond to the direct reflections from the rods while the signals arriving later are due to multiple scattering between the rods. Moreover, the time traces around the 150th element contain a single wavepacket because one of the rods is placed in the acoustic shadow of the other.

The structure of the eigenvalues of the T_∞ operator is shown in Fig. 14. In this case the transition between dominant and nondominant eigenvalues occurs around the 135th eigenvalue. For two impenetrable cylinders the expected value of dominant eigenvalues is $2(2ka+1) \approx 122$ which is close to the estimated value. The image of the rods obtained with the FM is shown in Fig. 15. It can be observed that thanks to the relatively large wavelength (1.78 mm) the grating lobes are suppressed (compare with Fig. 6).

Figure 16 provides a comparison between the FM and the KM method. The appearance of internal, concentric rings is due to the symmetry of the scatterers (see the Appendix). As it has already been pointed out, the rings can be removed by applying a threshold. Note that due to the large glass-water impedance contrast the two rods can be considered as sound-hard; therefore, the hollow rods actually behave as solid rods. Overall, the FM provides an accurate reconstruction of the two rods boundaries. In contrast, the KM image shown in Fig. 16(b) contains large sidelobes in the form of concentric rings which interfere with the edges of the rods. In particular, the image of the rod on the left side of Fig. 16(b) is not an exact circular shape. Moreover, there are portions of the rod contours which are not reconstructed [see arrows in Fig. 16]. These artifacts are due to the acoustic shadow which is

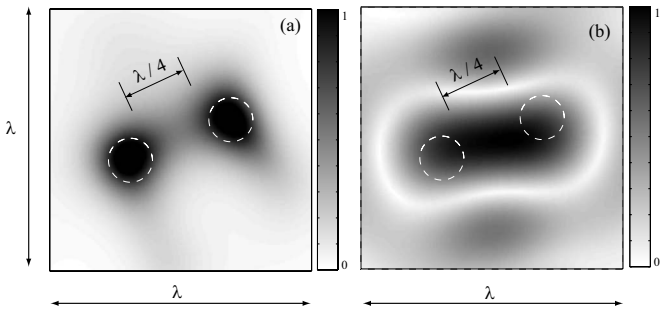

FIG. 12. Monochromatic images of the wires at 1 MHz ($\lambda = 1.5$ mm). (a) Factorization method; (b) Kirchhoff migration. The circles represent the actual size and position of the wires.

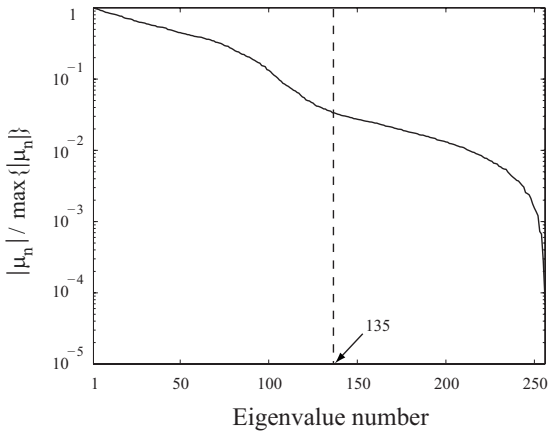

FIG. 14. Eigenvalues of the measured far-field operator at 850 kHz for the two-rod experiment.

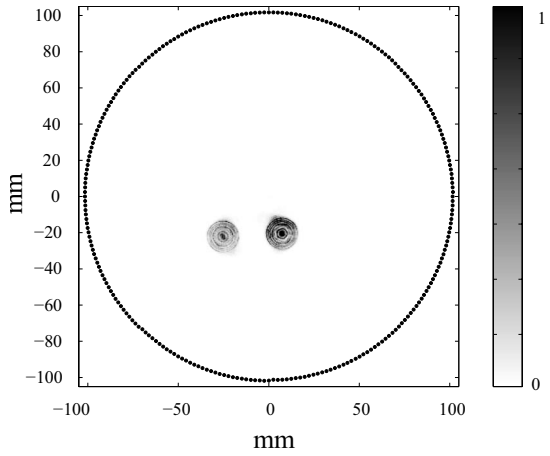

FIG. 15. Monochromatic image of the two rods at 850 kHz obtained with the factorization method.

caused by multiple scattering. Under the Born approximation, the field scattered by the two rods is the same as the superposition of the fields scattered by each rod separately. The KM method reconstructs the images by extracting the signals associated with the scattering from each rod and combining them according to Eq. (19). However, due to the shadowing effect, part of these signals are missing (see the pulse-echo signals around element 150, Fig. 13), resulting in the missing portions of the rod boundaries observed in Fig. 16(b).

VI. CONCLUSIONS

The scattering model used to describe the interaction of a probing wave with the structure of an object, is the key factor determining the amount of structural information that can be retrieved from scattering measurements. Conventional imaging methods are based on the Born approximation which neglects the distortion of the probing wave as it travels through the object to be imaged. Although the approximation leads to a linear mapping between the measurements and the structure of the object, the resolution of the reconstruction is limited by the $\lambda/2$ constraint. Moreover, the reconstruction can suffer from severe artifacts when strong multiple scattering occurs.

In this paper, it has been shown that by abandoning the Born approximation and considering a more accurate model which can account for multiple scattering effects, images with an unprecedented resolution better than $\lambda/4$ and with fewer artifacts than those observed under the Born approximation, can be achieved. This has been shown by using the factorization method.

The algorithm has been applied to experimental data obtained with an ultrasound ring array. Both objects smaller and larger than the wavelength have been imaged. It has been shown that the sampling methods can reconstruct the shape of extended scattering objects probed with ultrasonic waves.

It has been emphasized that due to the intrinsically ill-posed nature of the nonlinear inverse scattering problem, regularization techniques are needed to control the instability of the inverse problem which is triggered by measurement noise. In particular, it has been shown that the factorization, method is extremely robust against noise, providing super resolution in spite of a signal-to-noise-ratio lower than 0 dB.

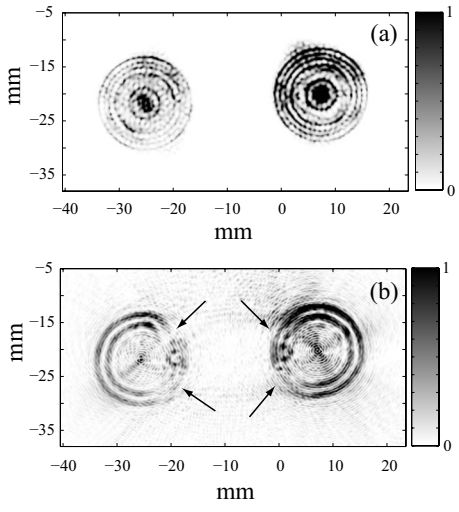

FIG. 16. Monochromatic images of the two rods at 850 kHz ($\lambda = 1.78$ mm). (a) Factorization method; (b) Kirchhoff migration. The arrows in (b) indicate the portions of the rod boundaries which have not been reconstructed.

ACKNOWLEDGMENTS

This work was supported through the U.S. DOE Laboratory-Directed Research and Development program at Los Alamos National Laboratory. F.S. is also grateful to the UK Royal Academy of Engineering / Engineering and Physical Sciences Research Council for supporting this work.

APPENDIX: CONCENTRIC RINGS

The presence of circular rings in Fig. 6(a) and Fig. 16 is due to the circular symmetry of the scatterers and the nature of the FM. This can be explained by considering the reconstruction of a single cylinder with the pseudospectrum (17). Let us consider the product $|\langle g_{\mathbf{z}}|v^n\rangle|$ calculated for an imaging point $\mathbf{z}$ with cylindrical coordinates (ψ,ρ). Since the problem is axisymmetric the eigenfunctions $|v_{\mathbf{z}}^n\rangle$ are given by Eq. (8), thus

$$\langle g_{\mathbf{z}}|v^n\rangle = \frac{1}{2\pi}\int_0^{2\pi} d\theta\, e^{-ik\rho\cos(\psi-\theta)}e^{in\theta}. \tag{A1}$$

By making the substitution $\alpha=\theta-\psi$ and invoking the Jacobi-Anger expansion

$$e^{iz\cos\alpha} = \sum_{m=-\infty}^{+\infty} i^m j_m(z)e^{im\alpha}, \tag{A2}$$

and exploiting the orthogonality of the functions $e^{in\theta}$ in $[0,2\pi]$ one obtains

$$\langle g_{\mathbf{z}}|v_{\mathbf{z}}^{n}\rangle = i^{n}\frac{e^{in\psi}}{2\pi}j_{n}(k\rho), \tag{A3}$$

where $j_n(\cdot)$ are the nth order Bessel functions of the first kind. As a result, the quantity $|\langle g_{\mathbf{z}}|v^{n}\rangle|$ is independent of the angular position of the imaging point ψ. For large orders n, the Bessel functions exhibit an oscillatory behavior along the radial direction for $k\rho > n$ whereas they rapidly tend to zero for $k\rho \to 0$. As a result, the Bessel functions of order $\nu < 2\pi R/\lambda$, where R is the cylinder radius, provide the main contribution to the series in Eq. (17) evaluated within the cylinder support, i.e.,

$$\mathbf{z} \in D \Rightarrow, P(\mathbf{z}) \simeq 4\pi\left(\sum_{n=1}^{\nu}\frac{j_{n}(k\rho)^{2}}{\mu_{n}}\right)^{-1}. \tag{A4}$$

$P(\mathbf{z})$ oscillates along the radius because it depends on the sum of a finite number of oscillatory functions. Moreover, since $P(\mathbf{z})$ does not depend on the angular position, ψ, the radial oscillations result in the concentric rings observed in Figs. 6 and 16. As a last remark, it has to be stressed that FM requires the divergence of the series in Eq. (17) outside the scatterer support. The divergence would ensure the reconstruction of the object with unlimited contrast and resolution, regardless of the value of $P(\mathbf{z})$ within the scatterer support. However, due to the finite number of measurements and the presence of noise the series converges also outside the scatterer so limiting the contrast between the object and the background.

[1] E. Wolf, Opt. Commun. **1**, 153 (1969).
[2] F. Simonetti, Phys. Rev. E **75**, 048602 (2007).
[3] F. Simonetti, Phys. Rev. E **73**, 036619 (2006).
[4] J. Hadamard, *Lectures on Cauchy's Problems in Linear Partial Differential Equations* (Yale University Press, New Haven, 1923).
[5] F. C. Chen and W. C. Chew, Appl. Phys. Lett. **72**, 3080 (1998).
[6] F. Simonetti, Appl. Phys. Lett. **89**, 094105 (2006).
[7] F. Lin, A. I. Nachman, and R. C. Waag, J. Acoust. Soc. Am. **108**, 899 (2000).
[8] D. Colton and R. Kress, Inverse Probl. **22**, R49 (2006).
[9] A. Kirsch, Inverse Probl. **18**, 1025 (2002).
[10] K. Belkebir and M. Saillard, Inverse Probl. **17**, 1565 (2001).
[11] M. Born and E. Wolf, *Principles of Optics* (Cambridge University Press, Cambridge, UK, 1999).
[12] A. C. Kak and M. Slaney, *Computerized Tomographic Reconstruction* (IEEE Press, New York, 1999).
[13] G. B. Arfken and H. J. Weber, *Mathematical Methods for Physicists* (Academic Press, London, 2001).
[14] E. Gerjuoy and D. S. Saxon, Phys. Rev. **94**, 1445 (1954).
[15] A. O. Barut, *The Theory of the Scattering Matrix: For the Interactions of Fundamental Particles* (Macmillan, New York, 1967).
[16] D. Colton and R. Kress, *Inverse Acoustic and Electromagnetic Scattering Theory* (Springer-Verlag, Berlin, 1992), Vol. 93.
[17] S. Li and E. J. Heller, Phys. Rev. A **67**, 032712 (2003).
[18] B. J. Stoyanov and R. A. Farrell, Phys. Rev. E **54**, 6838 (1996).
[19] D. Colton and R. Kress, SIAM J. Appl. Math. **55**, 1724 (1995).
[20] F. Simonetti, L. Huang, and N. Duric, J. Appl. Phys. **101**, 083103 (2007).
[21] A. Kirsch, Inverse Probl. **14**, 1489 (1998).
[22] P. M. Morse and H. Feshbach, *Methods of Theoretical Physics* (McGraw-Hill Book Company, New York, London, 1953).
[23] L. Flax and L. R. Dragonette, J. Acoust. Soc. Am. **63**, 723 (1978).
[24] H. Überall, Acoust. Phys. **47**, 115 (2001).
[25] M. Dorbin and C. Savit, *Introduction to Geophysical Prospecting*, 4th ed. (McGraw-Hill, New York, 1988).
[26] L. Borcea, G. Papanicolaou, and C. Tsogka, Inverse Probl. **21**, 1419 (2005).
[27] M. Karaman, P.-C. Li, and M. O'Donnell, IEEE Trans. Ultrason. Ferroelectr. Freq. Control **42**, 429 (1995).
[28] D. Colton, J. Coyle, and P. Monk, SIAM Rev. **42**, 369 (2000).